GEOPHYSICS, VOL. 65, NO. 1 (JANUARY-FEBRUARY 2000); P. 148–157, 17 FIGS.

Incorporating geological dip information into geophysical inversions

Yaoguo Li* and Douglas W. Oldenburg‡

ABSTRACT

Geological bodies are often linear structures that have well-defined strike direction and dip angle. We develop a new model objective function that allows this important information to be incorporated into geophysical inversions. A rotation matrix is applied to the horizontal and vertical derivatives of the model so that the derivative in an arbitrary direction is obtained. A model objective function that measures the flatness with respect to the rotated derivatives favors models that have elongated features with the specified strike and dip angle. Formulations for both 2-D and 3-D cases are presented, and they are illustrated using examples from dc resistivity and induced polarization (IP) problems. Synthetic and field examples show that an inversion carried out using known dip information produces a model that has higher resolution and provides a better representation of the true structure.

INTRODUCTION

The geophysical inverse problem is nonunique and is often solved by minimizing an unconstrained objective function of the form

$$\phi(m) = \phi_d(m) + \mu\phi_m(m), \tag{1}$$

where m denotes the model to be found, $\phi_d(m)$ is a data misfit function whose magnitude depends upon the difference between observed and predicted data, and $\phi_m(m)$ is a model objective function. The regularization parameter μ determines the trade-off between the data misfit and model objective function. Our optimization problem is solved by finding μ and a minimizer of equation (1) such that the observed data are fit to within the error tolerance (e.g., Tikhonov and Arsenin, 1977; Menke, 1984; Parker, 1994). The model objective function stabilizes the solution and provides a means to input prior information into the inversion so that a model is constructed with certain user-defined characteristics. One type of objective function we have used for inversion of many different geophysical data sets [e.g., dc resistivity and induced polarization (IP) (Oldenburg et al., 1993; Oldenburg and Li, 1994), magnetics (Li and Oldenburg, 1996), and gravity (Li and Oldenburg, 1998)] is comprised of a smallness component and first-order derivatives in spatial directions:

$$\begin{aligned}\phi_m(m) = {} & \alpha_s \int_V \{m(\vec{r}) - m_0\}^2 dv \\ & + \alpha_x \int_V \left\{ \frac{\partial [m(\vec{r}) - m_0]}{\partial x} \right\}^2 dv \\ & + \alpha_y \int_V \left\{ \frac{\partial [m(\vec{r}) - m_0]}{\partial y} \right\}^2 dv \\ & + \alpha_z \int_V \left\{ \frac{\partial [m(\vec{r}) - m_0]}{\partial z} \right\}^2 dv. \end{aligned} \tag{2}$$

In equation (2), m is a generic symbol denoting the model to be found (e.g., it can be the log conductivity in dc resistivity inversion or the chargeability in IP inversion) and m_0 is a reference model. The coefficients α_s, α_x, α_y, and α_z are positive constants that globally control the relative importance of the different terms. Only three of the four coefficients are independent; however, we retain all four for generality and convenience. To obtain a smooth model, α_s is usually chosen to be much smaller than the remaining three coefficients. By varying the relative magnitudes of α_x, α_y, and α_z, the inversion algorithm can construct models that are smoother, and thus more elongated, in one or two preferential directions among the three coordinate axes. For instance, choosing $\alpha_z \gg \alpha_x = \alpha_y$ will produce a model that has pipe-like features elongated vertically; and choosing $\alpha_z \ll \alpha_x = \alpha_y$ will produce a model that has sheet-like horizontal features. The following example illustrates the use of the coefficients in constructing different types of models.

Manuscript received by the Editor April 16, 1997; revised manuscript received September 3, 1999.
*Formerly Dept. of Earth and Ocean Sciences, Univ. of British Columbia, 129-2219 Main Mall, Vancouver, BC V6T 1Z4, Canada; currently Dept. of Geophysics, Colorado School of Mines, 1500 Illinois St., Golden, Colorado 80401. E-mail: ygli@mines.edu.
‡Dept. of Earth of Ocean Sciences, Univ. of British Columbia, 129-2219 Main Mall, Vancouver, BC V6T 1Z4, Canada. E-mail: doug@geop.ubc.ca.

For simplicity, we consider a 2-D dc resistivity problem in which the strike direction of the model is aligned with the y-axis. The associated model objective function will include only the derivative terms in the x- and z-axis directions, and only the ratio α_x/α_z needs be considered. Figure 1 shows a synthetic conductivity model and the apparent conductivity pseudosection from a pole-dipole array. Data are contaminated with 5% uncorrelated Gaussian noise. Here and elsewhere in the paper we use the misfit function

$$\phi_d = \sum_{i=1}^{N} \left(\frac{d_i^{\text{obs}} - d_i^{\text{pre}}}{\epsilon_i} \right)^2, \tag{3}$$

where d_i^{obs} and d_i^{pre} are observed and predicted data, respectively, and ϵ_i is the standard deviation of the error. Each inversion was completed so that the final misfit was equal to $N = 116$, which is the number of data. Inverting this data set using different α_x/α_z ratios produces conductivity models with different smoothness characteristics, as shown in Figure 2. The recovered anomalies are nearly circular when $\alpha_x = \alpha_z$, and they are horizontally elongated when $\alpha_x > \alpha_z$ and vertically elongated when $\alpha_x < \alpha_z$. It is clear from the inversions in this example that dip is not constrained by the data.

Strike and dip are important structural information, and they can sometimes be obtained independently from other geophysical surveys or estimated from known geology. When such information is available, it is important that it be incorporated into geophysical inversions for then the final image will more closely resemble the real earth. Although the current algorithm using the objective function in equation (2) has the ability to generate structures that are elongated in the horizontal or vertical direction, it is not designed to generate structures with arbitrary dips. This is because the objective function in equation (2) depends only upon the squares of the derivatives; the directionality is lost.

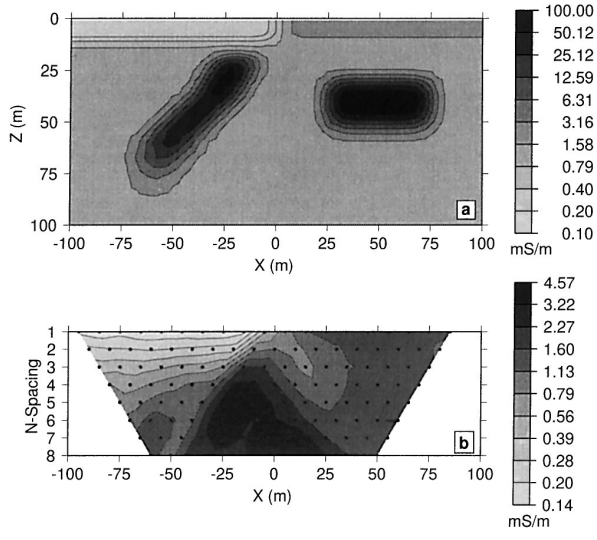

FIG. 1. (a) A synthetic conductivity model consisting of an overburden and two buried conductors with different dip angles. (b) The apparent conductivity pseudosection from a pole-dipole array with $a = 10$ m and $n = 1, 8$. The grayscale shows the conductivities in mS/m.

In the following, we introduce a modification to equation (2) by rotating the derivatives in a given coordinate system so that an arbitrary structural direction, such as strike and dip, can be incorporated into the inversion. Moreover, we divide the full model domain into subdomains so that preferential strike and dip can be assigned to each.

To generate a dipping objective function, we use the spatial derivatives of the model in the direction of the principal axes of the structure. Let

$$\begin{aligned}\phi_m(m) = \alpha_s \int_V \{m(\vec{r}) - m_0\}^2 dv \\ + \alpha_{x'} \int_V \left\{ \frac{\partial [m(\vec{r}) - m_0]}{\partial x'} \right\}^2 dv \\ + \alpha_{y'} \int_V \left\{ \frac{\partial [m(\vec{r}) - m_0]}{\partial y'} \right\}^2 dv \\ + \alpha_{z'} \int_V \left\{ \frac{\partial [m(\vec{r}) - m_0]}{\partial z'} \right\}^2 dv,\end{aligned} \tag{4}$$

where the derivatives are defined along the axes of the structural coordinates having directional vectors $(\hat{x}', \hat{y}', \hat{z}')$, which are aligned with the principal axes of the structure. The derivatives are obtained by combining the partial derivatives given in the axis directions of the user coordinates having directional vectors $(\hat{x}, \hat{y}, \hat{z})$:

$$\vec{g}_s = \mathbf{R}\vec{g}_u, \tag{5}$$

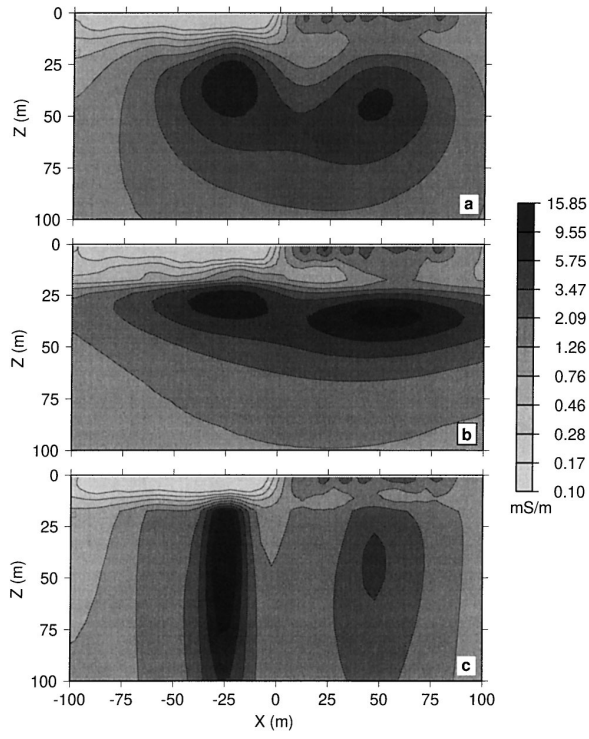

FIG. 2. Different conductivity models obtained from inverting the data in Figure 1b using different smoothness values: (a) $\alpha_x/\alpha_z = 1.0$; (b) $\alpha_x/\alpha_z = 100.0$; (c) $\alpha_x/\alpha_z = 0.01$.

where $\vec{g}_s = (\partial m/\partial x', \partial m/\partial y', \partial m/\partial z')^T$ is the gradient in the structure coordinates and $\vec{g}_u = (\partial m/\partial x, \partial m/\partial y, \partial m/\partial z)^T$ is the gradient in the user coordinate system. The matrix $\mathbf{R}$ depends upon the angles specifying the orientation of the structure in the user coordinates.

The user coordinate system is usually defined as having the z-axis pointing vertically downward and the x- and y-axes coinciding with the directions of the survey grid on the earth's surface. To specify the orientation of a general 3-D structure, two angles are needed to describe the strike and dip if only dike-like, or cylindrical, features are sought, and three angles are needed to fully describe a 3-D orientation if ellipsoidal features are sought. For 2-D models, only one angle that specifies the dip of the structure with respect to the positive x-axis is needed to define the orientation.

In the following sections we first present the 2-D dipping objective function, illustrate it with examples, and then extend the result to general 3-D models. Synthetic and field examples of dc resistivity and IP problems illustrate the new objective function for both cases. Since the IP inversion is a two-step process that depends upon the completion of inverting the dc resistivity data, we also examine the effect upon IP inversion when the dip is incorporated into the dc resistivity inversion.

2-D DIPPING OBJECTIVE FUNCTIONS

Define the user coordinates as $\hat{z}$ pointing vertically downward, $\hat{y}$ pointing along the strike, and $\hat{x}$ pointing horizontally on the earth's surface. Define a structure coordinate system by rotating $(\hat{x}, \hat{y}, \hat{z})$ about $\hat{y}$ clockwise such that $\hat{x}'$ is aligned with the dipping plane of the structure and points downward. Since the model is independent of the y-coordinate, we can remove the y-derivative term in equation (2) and reduce the volume integral to a surface integral performed over the x-z-plane. Using the partial derivatives in the structure coordinate system, the objective function can be written as

$$\phi_m(m) = \alpha_s \int_S \{m - m_0\}^2 ds + \alpha_{x'} \int_S \left\{ \frac{\partial [m - m_0]}{\partial x'} \right\}^2 ds + \alpha_{z'} \int_S \left\{ \frac{\partial [m - m_0]}{\partial z'} \right\}^2 ds. \quad (6)$$

Defining the dip angle of the structure, θ, as measured clockwise from $\hat{x}$, the rotation matrix is given by

$$\mathbf{R} = \begin{pmatrix} \cos\theta & \sin\theta \\ -\sin\theta & \cos\theta \end{pmatrix}. \quad (7)$$

From equation (5) we have

$$\begin{aligned} \frac{\partial m}{\partial x'} &= \frac{\partial m}{\partial x}\cos\theta + \frac{\partial m}{\partial z}\sin\theta, \\ \frac{\partial m}{\partial z'} &= -\frac{\partial m}{\partial x}\sin\theta + \frac{\partial m}{\partial z}\cos\theta. \end{aligned} \quad (8)$$

Substituting into equation (6) yields the desired dipping model objective function:

$$\begin{aligned} \phi_m(m) = \alpha_s &\int_S \{m - m_0\}^2 ds \\ &+ \int_S \left(\alpha_{x'}\cos^2\theta + \alpha_{z'}\sin^2\theta\right)\left\{ \frac{\partial [m - m_0]}{\partial x} \right\}^2 ds \\ &+ \int_S \left(\alpha_{x'}\sin^2\theta + \alpha_{z'}\cos^2\theta\right)\left\{ \frac{\partial [m - m_0]}{\partial z} \right\}^2 ds \\ &+ \int_S 2(\alpha_{x'} - \alpha_{z'})\sin\theta\cos\theta \frac{\partial [m - m_0]}{\partial x} \\ &\times \frac{\partial [m - m_0]}{\partial z} ds. \end{aligned} \quad (9)$$

The first three terms in equation (9) are the objective function in equation (6) (henceforth referred to as the generic objective function) with modified coefficients. The last term directly introduces the preferential weighting for a given dip. The dipping objective function reduces to the original function when $\alpha_{x'} = \alpha_{z'}$, which means there is no preferential weighting, or when $\theta = 0$ or $\theta = \pi/2$, which means the preferential direction is aligned with one of the axes in the user coordinate system.

In practical applications, we would like to incorporate different dip angles in regions of the subsurface. Thus, we divide the model domain into a number of subdomains and compose the total model objective function from components defined over these subdomains. Each region is assigned particular values of $(\alpha_s, \alpha_{x'}, \alpha_{z'}, \theta)$ such that the preferred dip is generated. This is illustrated in Figure 3. To accomplish this numerically, each cell is defined with its own set of values for $(\alpha_{sj}, \alpha_{x'j}, \alpha_{z'j}, \theta_j)$, where the subscript j denotes the index of cells in the model. The discretized objective function has the form

$$\begin{aligned} \phi_m(m) = (\vec{m} - \vec{m}_0)^T &\left[W_s^T W_s + D_x^T B_x D_x + D_z^T B_z D_z \right. \\ &\left. + \left(D_x^T B_{xz} D_z + D_z^T B_{xz} D_x\right) \right] (\vec{m} - \vec{m}_0), \end{aligned} \quad (10)$$

where

$$\begin{aligned} B_x &= \mathrm{diag}\left\{ \alpha_{x'j}\cos^2\theta_j + \alpha_{z'j}\sin^2\theta_j \big|_{j=1,M} \right\}, \\ B_z &= \mathrm{diag}\left\{ \alpha_{x'j}\sin^2\theta_j + \alpha_{z'j}\cos^2\theta_j \big|_{j=1,M} \right\}, \\ B_{xz} &= \mathrm{diag}\left\{ (\alpha_{x'j} - \alpha_{z'j})\sin\theta_j\cos\theta_j |_{j=1,M} \right\}, \end{aligned} \quad (11)$$

and D_x and D_z are the matrix representations of finite-difference operators. All the derivatives are defined at the centers

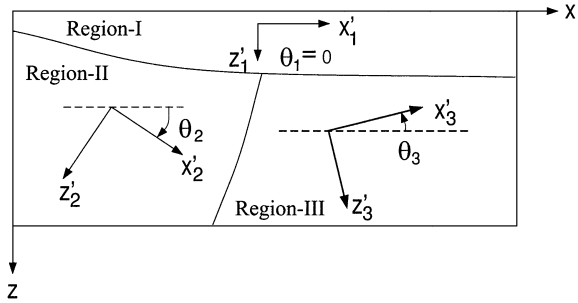

FIG. 3. Different dip angles can be input for different regions of the model; here, the model consists of three regions.

of the cells. The last term in equation (9) is represented by two matrix products in equation (10). This ensures that the composite weighting matrix is symmetric.

The objective function in equation (10) can now be used to construct models that have dipping structures. The user first needs to specify the angle θ. Then specifying $\alpha_{x'} > \alpha_{z'}$ in a region will favor linear structures having a dip angle of θ, and setting $\alpha_{x'} < \alpha_{z'}$ will produce structures that dip at an angle of $\pi/2 + \theta$. The latter is equivalent to specifying a dip angle of $\pi/2+\theta$ and $\alpha_{x'} > \alpha_{z'}$. Note that α's in equation (2) have a global effect, while α's in equation (10) are local and are specific to each region. Thus, to retain the global contribution of the smallness term to the total model objective function, the inversion should assign a constant α_s throughout the model domain and only vary the relative magnitude of $\alpha_{x'}$ and $\alpha_{z'}$ to achieve the desired dip. The value of α_s should be varied only if a different preference on the closeness to the reference model is sought in different regions. This is the justification for retaining all coefficients instead of only the independent ones in equation (2).

2-D NUMERICAL EXAMPLES

We now apply the new objective function to the inversion of 2-D dc resistivity data. The first model is shown in Figure 1a. It consists of two conductors buried in a more resistive half-space beneath an overburden. The overburden on the left is more resistive than the half-space; on the right, the overburden is more conductive than the half-space. The buried conductor on the left has a dip angle of 135°, and the one on the right is horizontal. Assuming a surface pole-dipole array with the potential dipole on the right (PDR) and a dipole length of 10 m, we have simulated data between $x = (-100, 100)$. The data are shown as an apparent conductivity pseudosection in Figure 1b. We carry out a number of inversions by varying $\alpha_{x'}$, $\alpha_{z'}$, and θ. The reference model m_0 is a constant of 5 mS/m. In this and all synthetic inversions, the data have been contaminated with Gaussian noise (5% for dc potentials and 5% plus 0.001 for apparent chargeabilities). The correct standard deviations of the data are used in the inversion, and the final data misfit ϕ_d achieves the expected χ^2 value of 116.

Figure 4 compares the models recovered using generic and dipping objective functions. In Figure 4a the conductivity model is obtained by inverting the data using $\alpha_{x'} = \alpha_{z'}$ and $\theta = 0$. The model clearly shows the two sections of the overburden layer and the two buried conductors. However, the conductors appear as nearly circular highs within a broad conductive anomaly. There is no indication of dip since this is not unequivocally demanded by the data. Figure 4b is the model recovered using an objective function that incorporates three regions of different dip angles. The region below $z = 20$ m and west of $x = 0$ m has $\theta = 135°$ and $\alpha_{x'}/\alpha_{z'} = 1000$, and the region below $z = 20$ m and east of $x = 0$ m has $\theta = 0°$ and $\alpha_{x'}/\alpha_{z'} = 20$. The rest of the model domain has no dip incorporated, and α_s remains constant throughout the model. The recovered model now shows a dipping conductor on the left and a horizontal conductor on the right. There is clear separation between the two conductors, and the dipping conductor yields a good estimate of the position of the true conductor. The overburden is basically the same as that in Figure 4a, since no special weighting has been applied in that region. This inversion shows the effectiveness of the new model objective function, and it illustrates the potential benefits that can be gained by including dip information in the geophysical inversion.

Next, we invert the induced polarization data generated from a chargeability distribution associated with the above conductivity model. The chargeability model is shown in Figure 5a, and the apparent chargeability pseudosection is displayed in Figure 5b. IP inversion uses the conductivity model recovered from dc resistivity data for sensitivity calculation; therefore, it is dependent upon the details of preceding dc resistivity inversion. Three different inversions are performed using conductivities from generic and dipping objective functions: (1) both dc resistivity and IP inversions use generic objective function; (2) dc resistivity inversion uses the generic objective function but IP inversion uses a dipping objective function; (3) the same dipping objective function is used in both dc resistivity and IP inversions. The results are displayed in Figure 6. The second inversion can be viewed as assuming no structural correlation between the conductivity and chargeability distributions, while the third inversion assumes that the conductivity and chargeability are structurally correlated. Although some obvious artifacts are created, the use of a dipping objective function only in the IP inversion is able to construct dipping anomaly in the region where it is expected, and the incorporation of the dip information in both dc resistivity and IP inversions produces a sharper image of the dipping anomaly.

As a second example, we investigate the improvement in resolution gained from incorporating the dip information. A set of pole-dipole data with $a = 10$ m and $n = 1, 8$ was generated from the conductivity model shown in Figure 7a, which consists of two parallel, conductive dikes whose dip angle is

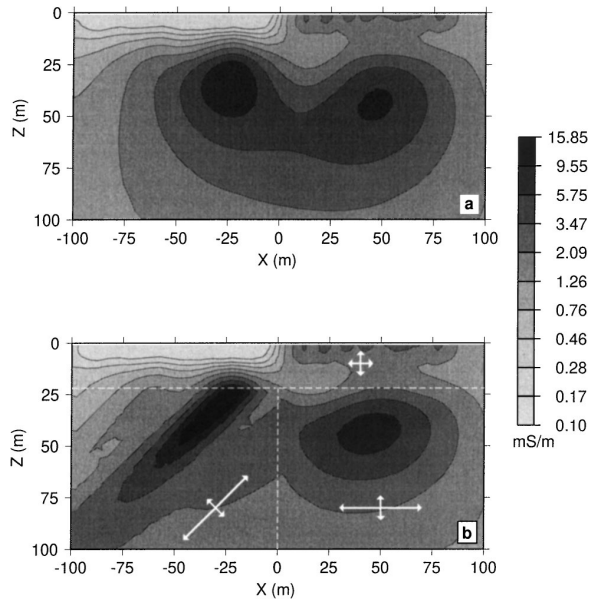

FIG. 4. Comparison of conductivity models recovered from the data in Figure 1b by using a generic objective function (a) and a dipping objective function with three different regions (b). The dashed lines indicate the boundaries between different regions. The arrows within identify the principal axes of the structure and the lengths of the arrows indicate qualitatively the relative weighting $\alpha_{x'}/\alpha_{z'}$.

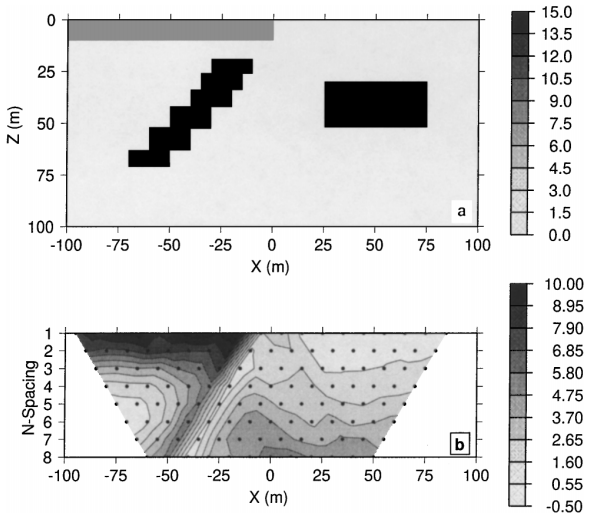

FIG. 5. (a) A chargeability model associated with the conductivity model in Figure 1a. The chargeability of the buried bodies is 0.15, and the surface layer is 0.1. The apparent chargeability from the same pole-dipole array is shown as a pseudosection in (b). The grayscale shows the chargeability multiplied by 100.

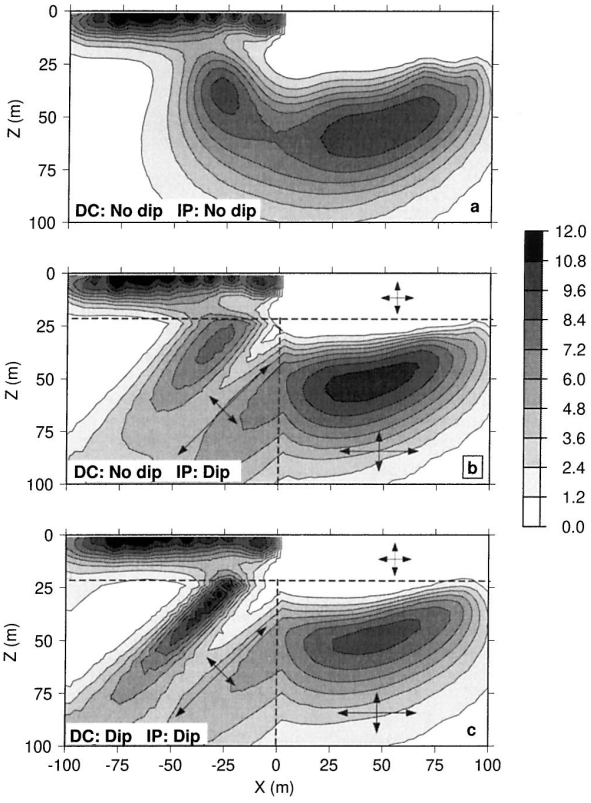

FIG. 6. Different chargeability models recovered by inverting the apparent chargeability in Figure 5b: (a) both dc and IP inversion use a generic (no dip) objective function; (b) dc inversion uses a generic objective function, but IP inversion uses a dipping objective function; (c) both dc and IP inversions use a dipping objective function. The different regions and their dipping directions are marked in the two lower panels.

135°. This model is similar to the one used by Coggon (1973) to compare the resolution of different arrays. The conductivity of the dike on the left is 25 mS/m, while that on the right is 50 mS/m. The depth to the top of the two dikes is 20 m; they are separated by a horizontal distance of 30 m, and each is 20 m wide. There is also a conductive overburden whose thickness is 10 m. The conductivity is then smoothed to complete the model. The noise-contaminated data are shown as an apparent conductivity pseudosection in Figure 7b. The data only show a broad, conductive anomaly, and there is no indication of two dipping conductors.

Carrying out inversion without dip weighting produces the conductivity model in Figure 8a, which shows a conductive overburden and a single buried conductor. There is some variation in the depth to the top of the conductor, but nothing indicates the presence of two conductors and their dipping structure.

Now, assume that we have information suggesting a dip angle of 135° below the overburden. We can incorporate that information into the inversion by assigning a ratio of $\alpha_{x'}/\alpha_{z'} = 1000$ everywhere below the overburden. The resulting model is shown in Figure 8b. Two conductors are clearly visible, and their locations and separation agree well with those of the true model. With the addition of dip information, the inversion is able to resolve the two anomalies, which would otherwise be interpreted as a single conductor.

Of course, a natural question is what happens if the inversion incorporates a dip that differs from the true dip. To see this, we inverted the same data by assuming that the dip angle is $\theta = 45°$. The resulting model is shown in Figure 8c, and it has only a broad conductor dipping at approximately 45°. Examining the three inverted models shows that the tops of the recovered conductivity anomalies are at the same depth. This indicates that the data contain enough information to resolve the tops of the conductors but not their dips or depth extents.

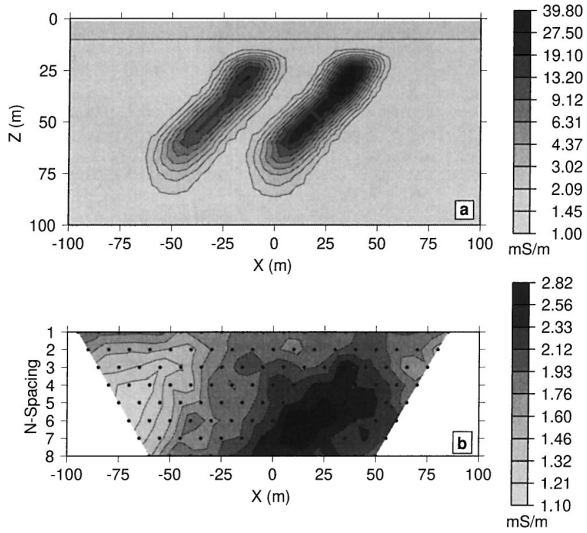

FIG. 7. A synthetic example consisting of two parallel dipping conductors beneath an overburden. (a) The model; (b) the apparent conductivity pseudosection from a pole-dipole array with $a = 10$ m and $n = 1, 8$.

An appropriate objective function, based upon the geological dip information, is needed to reconstruct the deeper portion of the model.

To test the effect of the array's depth penetration, we conducted the same experiments using data from arrays with a 20-m dipole length. For brevity, we have not produced the results here, but inverting those data has yielded similar models, as shown in Figure 8. Although the large array separation gives greater depth of penetration, it does not provide increased constraint on the dip of the subsurface structure. This is consistent with our observation that 2-D dc resistivity data acquired along a single traverse are not very sensitive to the dip. We conclude that the result depicted in Figure 8 is not limited to data sets with small depth of penetration.

Both models from the inversions using the opposite dip angles are valid since they reproduce the observations to the same degree. Shown in Figure 9 are the misfit maps corresponding to the three inversions in Figure 8. All three misfit maps are reasonably random, and there is little indication of which might constitute a better inversion. If one has no knowledge about geologic dip, then each of the three models represents a possible description of the true structure. Only when additional information is provided can one make a choice. For instance, if one knows that the geology is dipping to the left, the model in Figure 8b would be more favorable, and we can then infer that there are two separate conductors. Conversely, if we know that there are two separate units, then the same model would again be favorable; the fact that setting $\theta = 135^\circ$ produces two anomalies suggests that the geology is likely dipping to the left.

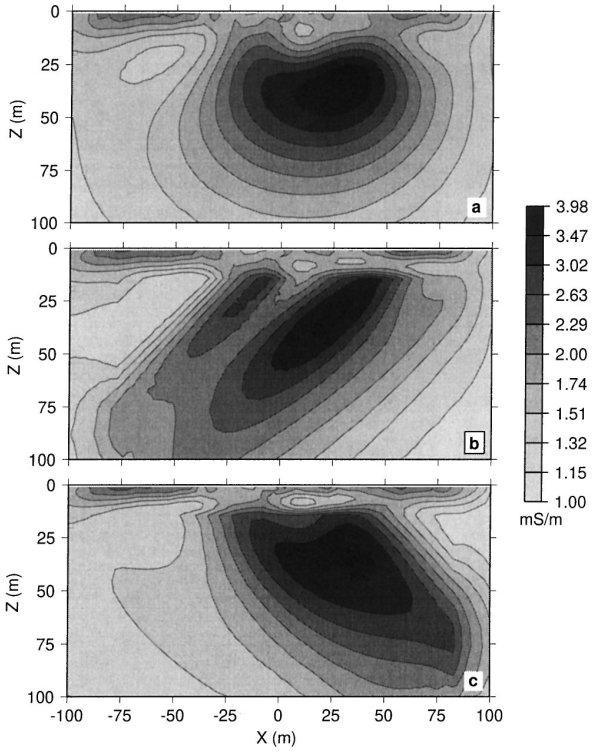

FIG. 8. Comparison of conductivity models recovered from the data in Figure 7b by using a generic objective function (a) and a dipping objective function (b and c). Panel (b) assumes a dip of 135° and shows that the correct dip information has helped to resolve the two conductors. Panel (c) assumes a dip of 45°, and the resulting conductivity illustrates the effect of incorrect dip angles.

3-D DIPPING OBJECTIVE FUNCTION

Define the user coordinates as $\hat{z}$ pointing vertically downward, $\hat{x}$ and $\hat{y}$ pointing respectively to nominal northing and easting directions of the survey. Define a structure coordinate system such that the $\hat{x}'$-$\hat{z}'$ plane is parallel to the dipping plane of geological bedding or structure and $\hat{x}'$ is aligned with the direction of the major axis. The objective function is defined by equation (4). The specification of an orientation in 3-D space is more difficult to visualize than that in 2-D space. We define the orientation of a 3-D object by three angles $(\varphi,\ \theta,\ \psi)$, where φ is the strike defined as the angle from the northing, θ is the dip measured downward from the horizontal plane, and ψ is the tilt that specifies the rotation of the object within its dipping plane. The reason for adopting tilt instead of the more commonly used plunge is that the strike direction defined as the intersection of the dipping plane and the earth's surface is constant under arbitrary tilt angle so that the intended strike φ is preserved. Figure 10 illustrates this set of angles by rotating a rectangular sheet that is vertical and striking north to the final position defined by the angles. The rotation is accomplished in three steps: rotation with respect to the z-axis by φ gives the desired strike; rotation with respect to the newly defined x'-axis by $(90-\theta)$ gives the dip angle of θ; and rotation about the latest y'-axis by ψ yields the desired tilt. Although we develop the objective function for a general 3-D structure defined by three angles, most practical applications are likely to use only

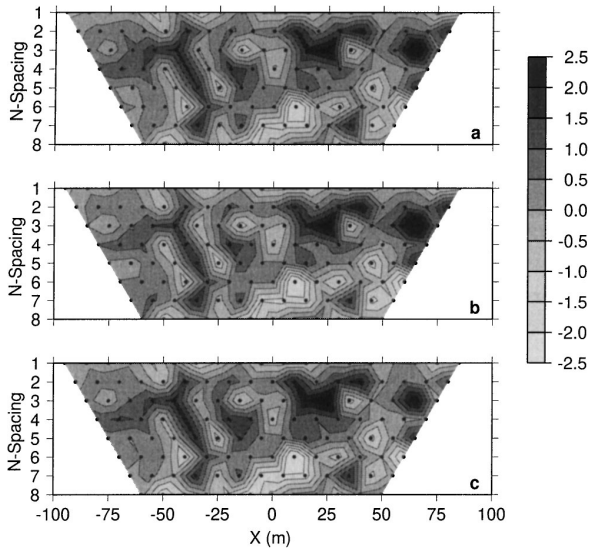

FIG. 9. Data-misfit maps corresponding to the three inversions shown in Figure 8. The quantity displayed in each panel is the difference between observed and predicted data normalized by the standard deviation of the error. All three inversions reproduce the observations to exactly the same misfit value. The misfit maps are very similar and appear to be sufficiently random.

the first two angles so that the dip can be incorporated perpendicular to the correct strike direction. In such cases, the tilt can be set to zero.

Given the above definition of the rotation angles, the rotation matrix **R** is defined by the concatenation of three 2-D rotation matrices in the order in which the rotations are applied. The final expression is given by

$$R = \begin{pmatrix} \cos\varphi\cos\psi - \sin\varphi\cos\theta\sin\psi & \sin\varphi\cos\psi + \cos\varphi\cos\theta\sin\psi & \sin\theta\sin\psi \\ -\sin\varphi\sin\theta & \cos\varphi\sin\theta & -\cos\theta \\ -\cos\varphi\sin\psi - \sin\varphi\cos\theta\cos\psi & \sin\varphi\sin\psi + \cos\varphi\cos\theta\cos\psi & \sin\theta\cos\psi \end{pmatrix} \equiv \begin{pmatrix} r_{11} & r_{12} & r_{13} \\ r_{21} & r_{22} & r_{23} \\ r_{31} & r_{32} & r_{33} \end{pmatrix}. \tag{12}$$

Thus, the derivatives in the structural coordinates are given by

$$\begin{pmatrix} \frac{\partial m}{\partial x'} \\ \frac{\partial m}{\partial y'} \\ \frac{\partial m}{\partial z'} \end{pmatrix} = \begin{pmatrix} r_{11}\frac{\partial m}{\partial x} + r_{12}\frac{\partial m}{\partial y} + r_{13}\frac{\partial m}{\partial z} \\ r_{21}\frac{\partial m}{\partial x} + r_{22}\frac{\partial m}{\partial y} + r_{23}\frac{\partial m}{\partial z} \\ r_{31}\frac{\partial m}{\partial x} + r_{32}\frac{\partial m}{\partial y} + r_{33}\frac{\partial m}{\partial z} \end{pmatrix}. \tag{13}$$

Substituting into equation (4) yields the desired 3-D dipping objective function,

$$\begin{aligned} \phi_m(m) = & \int_V \alpha_s m^2\, dv \\ & + \int_V \left(\alpha_{x'} r_{11}^2 + \alpha_{y'} r_{21}^2 + \alpha_{z'} r_{31}^2\right)\left(\frac{\partial m}{\partial x}\right)^2 dv \\ & + \int_V \left(\alpha_{x'} r_{12}^2 + \alpha_{y'} r_{22}^2 + \alpha_{z'} r_{32}^2\right)\left(\frac{\partial m}{\partial y}\right)^2 dv \\ & + \int_V \left(\alpha_{x'} r_{13}^2 + \alpha_{y'} r_{23}^2 + \alpha_{z'} r_{33}^2\right)\left(\frac{\partial m}{\partial z}\right)^2 dv \\ & + \int_V 2(\alpha_{x'} r_{11} r_{12} + \alpha_{y'} r_{21} r_{22} + \alpha_{z'} r_{31} r_{32})\frac{\partial m}{\partial x}\frac{\partial m}{\partial y}\, dv \\ & + \int_V 2(\alpha_{x'} r_{12} r_{13} + \alpha_{y'} r_{22} r_{23} + \alpha_{z'} r_{32} r_{33})\frac{\partial m}{\partial y}\frac{\partial m}{\partial z}\, dv \\ & + \int_V 2(\alpha_{x'} r_{11} r_{13} + \alpha_{y'} r_{21} r_{23} + \alpha_{z'} r_{31} r_{33})\frac{\partial m}{\partial x}\frac{\partial m}{\partial z}\, dv. \end{aligned} \tag{14}$$

We have omitted the reference model m_0 for brevity. The first four terms are the generic objective function with modified coefficients, and the last three terms directly introduce the strike, dip, and tilt.

For numerical solutions, the domain of the sought model is usually discretized by a 3-D orthogonal mesh, and the model is represented by a set of cuboidal cells of constant value. Correspondingly, the objective function in equation (14) is approximated by a finite-difference representation. Each cell is assigned its own set of values for $(\alpha_{sj}, \alpha_{x'j}, \alpha_{y'j}, \alpha_{z'j}, \varphi_j, \theta_j, \psi_j)$, where the subscript j denotes the index of cells in the model. This again allows several regions of different strike, dip, and tilt to be included in the model. The discretized objective function has a form similar to that of the 2-D dipping objective function in equation (10).

We now apply the 3-D dipping objective function to a synthetic dc resistivity problem. The model consists of two conductors buried in uniform background beneath an overburden of variable conductivity. Figure 11 shows the perspective view of the model, in which the conductor on the left has a strike of 0° and a dip of 135° and the second conductor has a strike of 30° and a dip of 74°. Both have zero tilt. Surface pole-dipole data are calculated for arrays with $a = 50$ m and $n = 1$, 8 along eleven east–west traverses spaced 100 m apart. Independent Gaussian noise having standard deviation equal to 2% of each accurate datum is added. There are 1364 observations. Figure 12 shows two apparent conductivity pseudosections at $x = 400$, 500 m and a plan map at the spacing $n = 4$. We first invert the data using a generic model objective function without dip information. The inversion is carried out using a Gauss–Newton approach (Li and Oldenburg, 1997). The resultant model is displayed in Figure 13. The strike direction of each conductor is clearly shown in the plan section at depth 150 m (Figure 13c). In the cross-section, the conductors appear to be dipping, although they are very smooth and become almost circular at lower conductivity values. This is nonetheless a good representation of the true model.

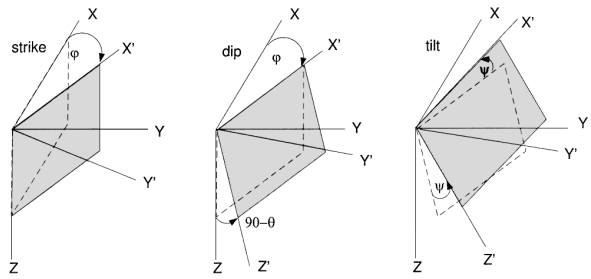

FIG. 10. Definition of the strike (φ), dip (θ), and tilt (ψ) that specify the orientation of the structural coordinates aligned with the principal axes of a 3-D object. The dashed lines indicate the position of the object before the particular rotation is applied. The user coordinates have axes (x, y, z), and the structural coordinates have axes (x', y', z').

We next invert the data using a 3-D dipping objective function. Three different regions are included: (1) the region above $z = 50$ m has no dip incorporated; (2) the region below $z = 50$ m and west of $y = 500$ m has $(\varphi, \theta, \psi) = (0^\circ, 135^\circ, 0^\circ)$ and $(\alpha_{x'}, \alpha_{y'}, \alpha_{z'}) = (10.0, 0.1, 10.0)$; and (3) the region below $z = 50$ m and east of $y = 500$ m has $(\varphi, \theta, \psi) = (30^\circ, 74^\circ, 0^\circ)$ and $(\alpha_{x'}, \alpha_{y'}, \alpha_{z'}) = (10.0, 0.1, 10.0)$. The resultant conductivity model is shown in Figure 14. The prisms clearly appear as tabular, dipping bodies in the cross-section, and the dip angles are very close to the true value. The inferred strike direction has not changed substantially. Overall, the recovered model has shown clear improvements as a result of incorporating the information about strike and dip of the true structure, and this model is a better representation of the true conductivity than that in Figure 13.

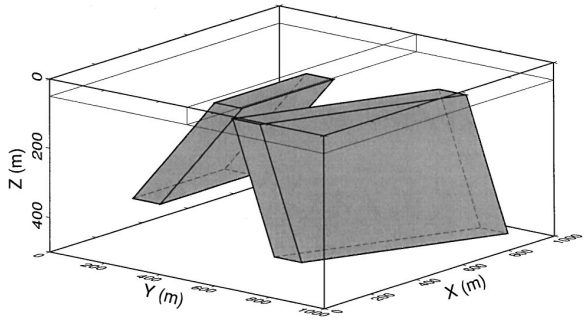

FIG. 11. A 3-D perspective view of the 3-D synthetic conductivity model. The conductors are represented by the gray-shaded blocks, and the overburden is represented by the light solid lines. The conductor on the left has a strike of 0° and a dip of 135°. It extends from $x = 300$ m to $x = 700$ m along strike and $z = 75$ m to $z = 400$ m at depth. The second conductor has a strike of 30° and dip of 74°; it extends from $x = 200$ m to $x = 800$ m along strike and $z = 75$ m to $z = 450$ m at depth. The half-space conductivity is 1 mS/m, while the overburden has a conductivity of 2 mS/m on the left and 0.5 mS/m on the right. The dipping conductors both have a conductivity of 100 mS/m.

In this example the strike direction is recovered very well by the generic inversion. This is true for most inversions of data that have good areal coverage. In such cases, the strike direction is evident in the data; incorporating the strike in the inversion only serves as a means to incorporate the dip.

FIELD EXAMPLE

To test the dipping objective function on field data, we invert a 2-D data set presented by Hallof and Yamashita (1990). The data were acquired over a gold deposit in Ontario. The deposit is associated with a steeply dipping sulfide body embedded in metasedimentary rock surrounded by volcanics. The formation

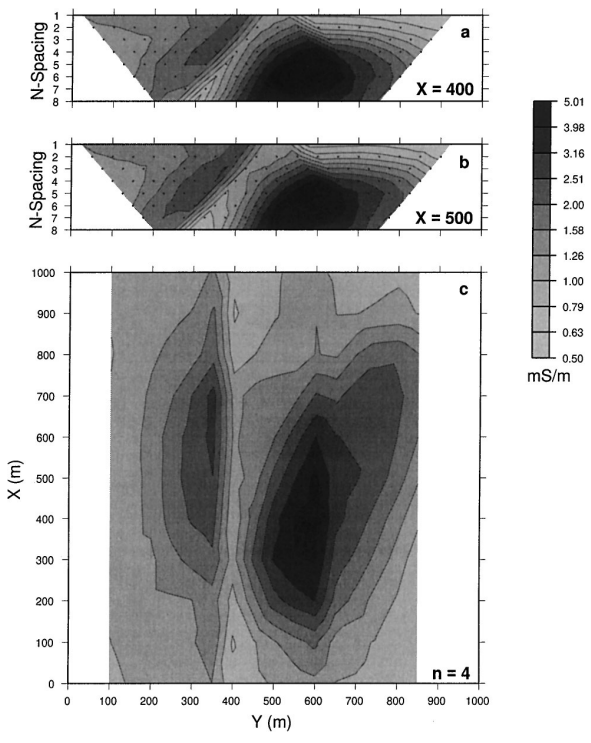

FIG. 12. Pole-dipole data are simulated for arrays with $a = 50$ m and $n = 1, 8$ along eleven east–west lines spaced 100 m apart. Apparent conductivity in two selected pseudosections at $x = 400$ m and 500 m, and in one plan section for $n = 4$ are shown in this figure. The grayscale indicates apparent conductivity in mS/m.

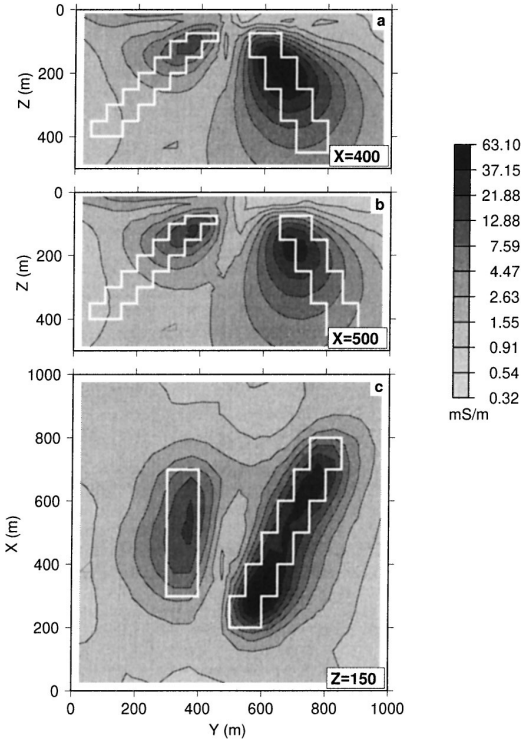

FIG. 13. A 3-D conductivity model recovered using a generic model objective function. The model is shown in two cross- sections and one plan section. The true positions of the conductors are outlined by the white boxes. The strike direction of each conductor is clearly shown in the plan section. In cross-section, the conductors appear as broad anomalies with some indication of their dipping nature. The grayscale indicates the conductivity in mS/m.

is overlain by a layer of glacial sediments of variable thickness. A dipole-dipole array with $a = 40$ m and $n = 1, 4$ is used. Figure 15 shows the apparent conductivity and IP phase pseudosections along with the geology. The dip angle of the sulfide body is estimated to be 110°.

Figure 16 displays the two inverted resistivity models using the generic and dipping objective functions, respectively. The generic objective function has $\alpha_x = \alpha_z$, whereas the dipping objective function has $(\alpha_x/\alpha_z = 8000)$ in the region below 30 m. The data are assigned errors of 5%. The main feature in these models is a conductive overburden of variable thickness. The dipping model displays some variations beneath the overburden, and the sharp change from the conductive to the resistive zone around $x = 50$ m appears to coincide with the boundary between the metasedimentary unit and the volcanics on the right. However, because of the limited depth of penetration, the variation at depth is poorly defined.

Three inverted IP phase models recovered using different objective functions are shown in Figure 17. We have assumed a constant error of 5% plus 2 mrad. The generic inversion using no dip information shows a concentrated IP high coinciding with the top of the mineralization zone. When the dip is incorporated into the IP inversion, the recovered anomaly shows an improved correspondence with the steeply dipping sulfide body and with the metasedimentary unit. The incorporation of dip information has provided better horizontal definition and has increased the depth extent of the body, which is compatible with known geology.

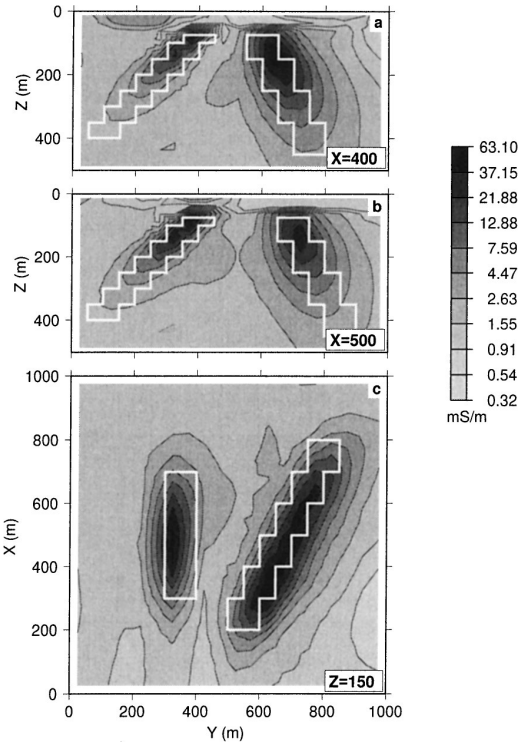

FIG. 14. A 3-D conductivity model recovered using a model objective function that incorporates the strike and dip of each conductor. The true position of the conductors is outlined by the white boxes. The recovered conductors dip at angles consistent with the respective true conductor.

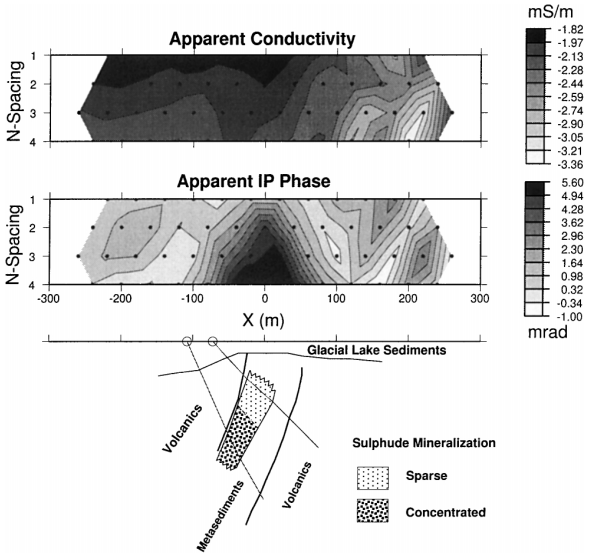

FIG. 15. A field data set reproduced with permission from Hallof and Yamashita (1990). The upper and middle panels show the apparent conductivity (in mS/m) and apparent IP phase (in mrad) pseudosections, respectively. The data were acquired using a dipole-dipole array with $a = 40$ m and $n = 1, 4$. The lower panel displays the geology and drillhole intersections.

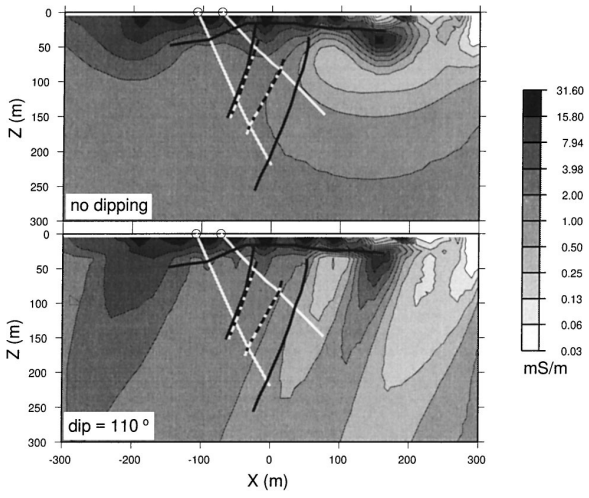

FIG. 16. Conductivity models recovered by inverting the dc resistivity data shown in Figure 15a using a generic model objective function (a) and a dipping model objective function (b), respectively. The geological boundaries and drillhole traces are shown by the overlays. Both models recover a conductive overburden of variable thickness; this corresponds with the glacial sediments. The variation at depth, however, is poorly defined because of the limited depth of penetration. The grayscale indicates the conductivity in mS/m.

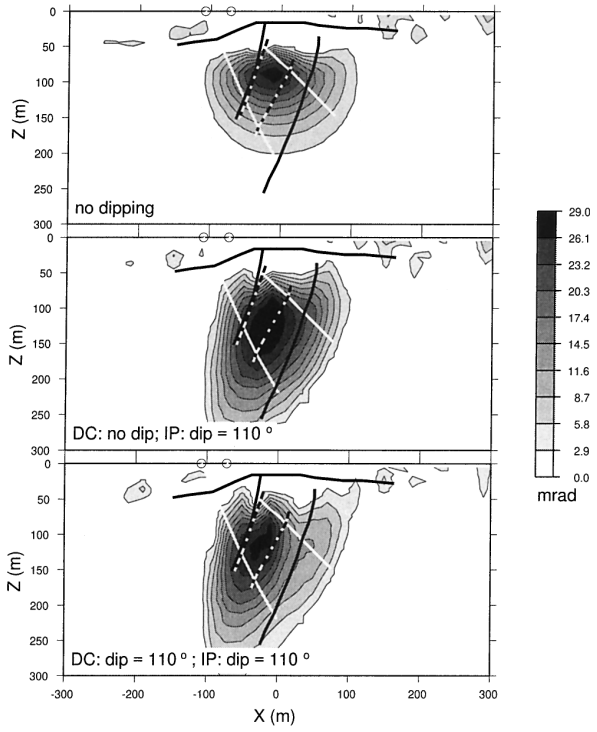

FIG. 17. Comparison of IP phase models (in mrad) recovered by inverting IP data shown in Figure 15b using different objective functions and background conductivity models. (a) A generic objective function and a generic conductivity used in Figure 16a. (b) A dipping model objective function for the IP inversion and a generic conductivity model used in Figure 16a. (c) A dipping model objective function and a dipping conductivity model used in Figure 16b.

CONCLUSION

Geophysical inversions are nonunique, and complementary information is often needed to reduce the ambiguity. Incorporating structural information such as dip angle helps construct a model that reflects known characteristics of the true geology. We have developed a new model objective function that includes strike and dip information about the geologic structure in multiple regions in our geophysical inversions. This additional information is particularly helpful in model regions that are poorly defined because of the data constraints. The resultant model is thus consistent with a priori geologic information and with data from the geophysical survey.

ACKNOWLEDGMENTS

We thank Roman Shekhtman for his assistance throughout this research project. Our discussions with Bob Smith, Tony Doe, and Tim Monks on the need to incorporate dip information prompted us to look into this problem. We also thank Dr. P. Fullagar and an anonymous reviewer for their comments that improved the clarity of the manuscript. This work was supported by an NSERC IOR grant and an industry consortium, Joint and Cooperative Inversion of Geophysical and Geological Data. Participating companies are Placer Dome, BHP Minerals, Noranda Exploration, Cominco Exploration, Falconbridge, INCO Exploration & Technical Services, Hudson Bay Exploration and Development, Kennecott Exploration Company, Newmont Gold Company, Western Mining Corporation, and CRA Exploration Pty.

REFERENCES

Coggon, J. H., 1973, A comparison of IP electrode arrays: Geophysics, **38**, 737–761.

Hallof, P. G., and Yamashita, M., 1990, The use of the IP method to locate gold-bearing sulfide mineralization, *in* Fink, J. B., Sternburg, B. K., McAlister, E. O., and Wieduwilt, W. G., Eds. Induced polarization: Applications and case histories: Soc. Expl. Geophys.

Li, Y., and Oldenburg, D. W., 1996, 3-D inversion of magnetic data: Geophysics, **61**, 394–408.

———1997, 3-D inversion of induced polarization data: Univ. of Arizona, Dept. of Mining and Geological Engineering, High-Resolution Geophysics Workshop, Expanded Abstract.

———1998, 3-D inversion of gravity data: Geophysics, **60**, 109–119.

Menke, W., 1984. Geophysical data analysis: Discrete inverse theory: Academic Press Inc.

Oldenburg, D. W., and Li, Y., 1994, Inversion of induced polarization data: Geophysics, **59**, 1327–1341.

Oldenburg, D. W., McGillivary, P. R., and Ellis, R. G., 1993, Generalized subspace method for large scale inverse problems: Geophys. J. Internat, **114**, 12–20.

Parker, R. L., 1994, Geophysical inverse theory: Princeton Univ. Press.

Tikhonov, A. N., and Arsenin, V. Y., 1977, Solutions of ill-posed problems: John Wiley & Sons, Inc.